

Carrier-driven coupling in ferromagnetic oxide heterostructuresChing-Hao Chang,¹ Angus Huang,² Sujit Das,^{1,3} Horng-Tay Jeng,^{2,4} Sanjeev Kumar,⁵ and R. Ganesh^{1,6,*}¹*Leibniz-Institute for Solid State and Materials Research, IFW-Dresden, D-01171 Dresden, Germany*²*Department of Physics, National Tsing Hua University, Hsinchu 30043, Taiwan*³*Institute for Physics, MLU Halle-Wittenberg, 06099 Halle, Germany*⁴*Institute of Physics, Academia Sinica, Taipei 11529, Taiwan*⁵*Indian Institute of Science Education and Research Mohali, Sector 81, S.A.S. Nagar, Manauli PO 140306, India*⁶*The Institute of Mathematical Sciences, HBNI, C I T Campus, Chennai 600 113, India*

(Received 18 January 2017; revised manuscript received 8 October 2017; published 7 November 2017)

Transition metal oxides are well known for their complex magnetic and electrical properties. When brought together in heterostructure geometries, they show particular promise for spintronics and colossal magnetoresistance applications. In this article, we propose a carrier-driven coupling mechanism in heterostructures composed of itinerant ferromagnetic materials. The coupling is mediated by charge carriers that strive to maximally delocalize through the heterostructure to gain kinetic energy. In doing so, they force a ferromagnetic or antiferromagnetic coupling between the constituent layers. To illustrate this, we focus on heterostructures composed of SrRuO₃ and La_{1-x}A_xMnO₃ (A = Ca/Sr). Using the minority-carrier nature of SrRuO₃, we provide a simple explanation for antiferromagnetic alignment that is known to occur in multilayers. We present a phenomenological Kondo-lattice model which reproduces the known magnetization properties of multilayers. In addition, we discuss a quantum well model for heterostructures and argue that the spin-dependent density of states determines the nature of the coupling. As a smoking gun signature, we propose that bilayers with the same constituents will oscillate between ferromagnetic and antiferromagnetic coupling upon tuning the relative thicknesses of the layers. We present *ab initio* results that support this prediction.

DOI: [10.1103/PhysRevB.96.184408](https://doi.org/10.1103/PhysRevB.96.184408)**I. INTRODUCTION**

Magnetic heterostructures have been intensively studied driven by the technological promise of spintronics [1] and colossal magnetoresistance [2]. Their interesting properties derive from the new physics that emerges when two different magnetic materials come into contact at an interface [3]. It is generally assumed that it is the interface that decides the coupling between layers and the overall properties of the heterostructure. For instance, ferromagnetic/antiferromagnetic alignments are usually attributed to superexchange interactions across the interface. In this article, we demonstrate a coupling mechanism driven by conduction electrons that diffuse deep into each constituent layer. Macroscopic behavior is determined not by the interface, but by the nature of charge carriers. Our study paves the way for tailoring spintronics devices with strongly coupled magnetic and transport properties.

To illustrate this coupling, we place our discussion within the context of heterostructures with alternating layers of SrRuO₃ (SRO) and La_{1-x}A_xMnO₃ (LAMO) with $x \sim 0.3$ and A = Ca/Sr. Both LAMO and SRO are layered metallic ferromagnets. While LAMO is a conventional double exchange system, SRO is a bad metal in which conduction is dominated by minority-spin electrons [4,5]. Multilayer SRO/LAMO heterostructures have been extensively studied with a view to understand the interlayer coupling. The typical M - T phase diagram has two sharp features [6]. Upon approaching from high temperatures, the LAMO layers first develop ferromagnetic order at $T_c^{\text{LAMO}} \sim 300$ K. Upon further

cooling, the SRO layers order in the opposite direction at $T_c^{\text{SRO}} \sim 150$ K and the net moment starts decreasing. The M - h curve shows three hysteresis loops [6,7], with the SRO layer flipping its ordered moment at some intermediate field. Taken together, these effects demonstrate antiferromagnetic coupling between the layers with a phase diagram as shown in Fig. 1. Density functional calculations performed at zero temperature also suggest antiferromagnetic coupling, attributing it to the role of interfacial oxygen atoms [6]. However, interfacial coupling does not provide a satisfactory mechanism as the constituent materials are metallic. Unlike Mott insulators with short-ranged superexchange couplings, itinerancy in metals invariably gives rise to long ranged interactions [8]. Bilayers of SRO and LAMO have also been studied, with several studies finding antiferromagnetic coupling [7,9–11].

We propose that the interlayer coupling in these systems is driven by charge carriers and not by interfacial Mn-O-Ru bonds. The key ingredient in our proposal is the minority carrier nature of SRO: its conduction electrons are predominantly polarized *opposite* to the direction of its ferromagnetic moment. On the other hand, LAMO, being a double exchange ferromagnet, has carriers which are polarized *parallel* to the ferromagnetic moment. An antiferromagnetic alignment of the ordered moments allows the conduction electrons to polarize the same way in both materials. Electrons can then maximally delocalize over the heterostructure and gain kinetic energy. This mechanism is clearly consistent with the antiferromagnetic ordering seen in multilayer heterostructures. In contrast, bilayers present a more nuanced situation depending on the density of states. We show that the carrier-driven mechanism predicts that the coupling will oscillate with the relative widths of layers.

*ganesh@imsc.res.in

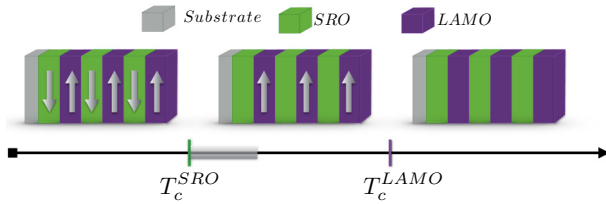


FIG. 1. Phase diagram of an SRO-LAMO multilayer heterostructure. The shaded regime above T_c^{SRO} has incipient ferromagnetic correlations in the SRO layers.

II. PHENOMONOLOGICAL MODEL FOR MULTILAYER GEOMETRIES

To describe multilayer heterostructures, we present a Kondo-lattice model of local moments coupled to itinerant electrons. Our objective is to show that the itinerancy of conduction electrons suffices to explain the nature of interlayer coupling, with no need for interfacial defects or interfacial superexchange couplings.

Our model consists of a square lattice divided into two regions, one with Mn and one with Ru ions, as shown in Fig. 2. Note that Mn and Ru are the magnetically active ions in LAMO and SRO, respectively. At each site, we have a local moment \mathbf{S}_i as well as an orbital that may be occupied by a conduction electron. The spin of the conduction electron at a given site is coupled to that of the corresponding local moment. The resulting Hamiltonian is given by

$$H = \sum_{i,\sigma,\sigma'} J_i \mathbf{S}_i \cdot \left\{ \frac{1}{2} c_{i,\sigma}^\dagger \vec{\tau}_{\sigma,\sigma'} c_{i,\sigma'} \right\} - \sum_{(ij),\sigma} \{ t_{ij} c_{i,\sigma}^\dagger c_{j,\sigma} + \text{H.c.} \} \\ + \sum_{i,\sigma} (\epsilon_i - \mu) c_{i,\sigma}^\dagger c_{i,\sigma} - h \sum_i \left\{ S_i^z + \frac{1}{2} \sum_{\sigma,\sigma'} c_{i,\sigma}^\dagger \tau_{\sigma,\sigma'}^z c_{i,\sigma'} \right\}. \quad (1)$$

The operator $c_{i,\sigma}^\dagger$ ($c_{i,\sigma}$) creates (annihilates) an itinerant electron at site i with spin σ . The components of $\vec{\tau}$ are Pauli matrices representing spin operators. We have included

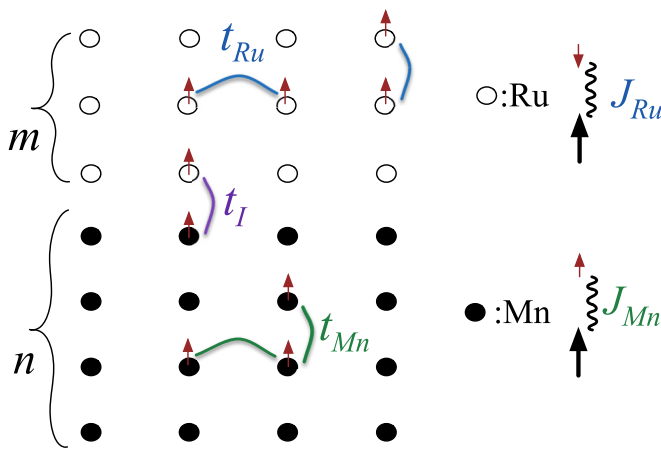


FIG. 2. A schematic view of the lattice model for n -LAMO/ m -SRO heterostructures. There are three different hopping parameters, t_{Mn} , t_{Ru} and t_I , and two different Kondo couplings, J_{Mn} and J_{Ru} .

an external magnetic field h . The parameters J_i and t_{ij} take different values within each material. The materials are coupled by hopping across the interface, with strength t_I . The local potential ϵ_i takes the value $\Delta(0)$ for Mn(Ru) sites. The relative on-site potential Δ is adjusted to achieve the desired average electronic density on SRO and LAMO sides.

A. Parameters appropriate for LAMO-SRO multilayers

We model the (n -LAMO/ m -SRO) multilayer as a cluster with m atomic layers of Ru and n atomic layers of Mn with overall periodic boundary conditions. Taking $t_{\text{Mn}} = 1$, we choose $t_{\text{Ru}} = 0.5$ to capture the relatively low value of T_c for SRO compared to LAMO. Along the interface, we fix the hopping t_I to be 0.5. The chemical potential μ and the relative on-site potential Δ are fixed so as to give an average electronic filling of 0.7 (0.5) for LAMO (SRO). We find the same qualitative results irrespective of the specific values of the parameters.

In SRO, the magnetic moments originate from Ru^{4+} ($4d^4$) ions residing in an octahedral crystal field. *Ab initio* calculations show that the valence electrons occupy t_{2g} orbitals, while the e_g orbitals remain empty [4,12,13]. In the atomic limit, the four electrons in the t_{2g} levels form a high-spin state with a total moment of $2 \mu_B/\text{Ru}$ atom. If two such atoms are brought together, the minority spins can hop between atoms, whereas the majority spin carriers will be localized due to Pauli blocking. As several atoms are brought together to form the material, itinerancy effects reduce the total moment on each Ru site to $\sim 1.5 \mu_B/\text{Ru}$ atom [4]. We model the Ru site as a $2 \mu_B$ local moment coupled to itinerant electrons, with an average filling of 0.5 per site. The Kondo coupling is taken to be positive ($J_{\text{Ru}} > 0$) to account for the minority carrier nature. DFT+DMFT studies also point to a dual nature of magnetism in SRO consisting of a Stoner behavior as well as local magnetic moments above T_c [14–16]. We note that a realistic description of SRO requires a multiorbital model with easy axis anisotropy, spin-orbit coupling, etc. However, our simple one-orbital model captures the essential aspect required for the carrier-driven mechanism, which is the minority carrier character.

In LAMO, on the other hand, the Mn ions are nominally in the $+3$ ($3d^4$) state. Three electrons with parallel spins occupy the t_{2g} levels, while the fourth electron occupies an e_g orbital. In undoped LaMnO_3 , superexchange drives the net $S = 2$ spins to order antiferromagnetically (the e_g orbital degree of freedom also orders). Replacing a fraction of the La atoms by Sr or Ca, removes electrons from the e_g levels and gives rise to the classic double exchange scenario. The filled t_{2g} electrons form a $S = 3/2$ local moment. The e_g electrons can maximally delocalize when the local moments order ferromagnetically. With this picture in mind, we assume a local moment of $3 \mu_B/\text{Mn}$ site. The Kondo coupling is negative ($J_{\text{Mn}} < 0$) reflecting the standard double exchange scenario. This scenario is well established in the context of bulk manganites [17,18]. In particular, in the optimally doped regime, $x \sim 0.3$, a single-band ferromagnetic Kondo lattice model can describe the magnetic and transport properties very well [19–21]. We fix J_{Mn} to be -20 and present results for different values of J_{Ru} .

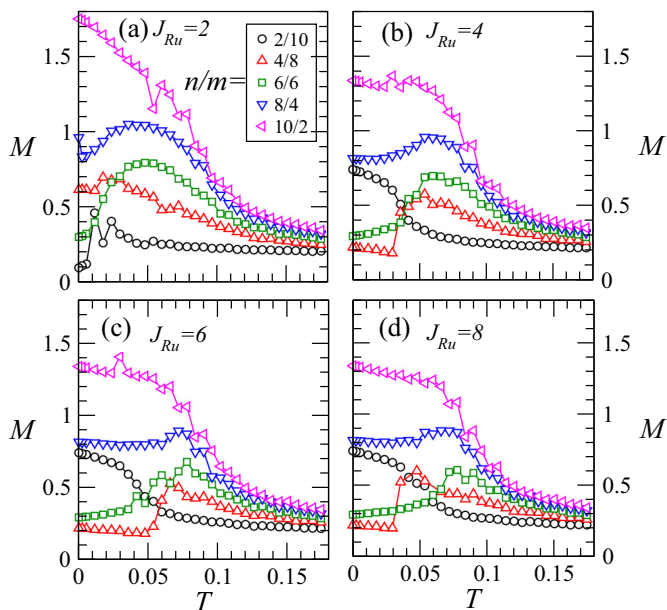


FIG. 3. (a)–(d) Magnetization as a function of temperature for different values of J_{Ru} . Each panel shows results for different relative thicknesses of LAMO-SRO layers as indicated by n/m . n and m are the number of LAMO and SRO rows in the unit cell, respectively, with $(n + m) = 12$ fixed. The results are obtained on a 4×12 lattice with periodic boundary conditions. The value of J_{Mn} is fixed to be -20 .

B. Semiclassical Monte Carlo simulations

To solve for the properties of the model, we use a protocol involving exact diagonalization of the conduction electrons combined with classical Monte Carlo sampling of the local moment configurations (see the Supplemental Material in Ref. [22] for details). Unlike *ab initio* calculations, this method is ideally suited to explore finite temperature properties. These computations are CPU intensive and therefore restricted to small clusters; however, they allow for an unbiased exploration of magnetic configuration space. We present results for the magnetization, defined as $\frac{1}{N_{av}} \sum_{\alpha} |M_{\alpha}|$, where N_{av} is the number of Monte Carlo configurations used for averaging. M_{α} is the magnetization for each configuration, defined as

$$M_{\alpha} = \frac{1}{N} \sum_i (\mathbf{S}_i + \langle \vec{\tau}_i \rangle), \quad (2)$$

where N is the total number of sites and angular brackets denote the quantum expectation values. Our results for magnetization vs temperature are plotted in Fig. 3, for different values of J_{Ru} and different relative widths of SRO and LAMO layers. As long as $J_{Ru} \geq 4$, we find the same qualitative behavior. For example, for a given choice of layer widths, the $T \rightarrow 0$ values of total magnetization are identical for $J_{Ru} = 4, 6, 8$.

While our simulations on small clusters cannot capture thermodynamic phase transitions, they show features that are indicative of phase transitions. The inflection points in the magnetization curve provide a first estimate of T_c . This can be taken as the temperature below which the correlation length exceeds the cluster size. With our parameters, we find $T_c^{LAMO} \sim 0.1t_{Mn}$ and $T_c^{SRO} \sim 0.04t_{Mn}$. In the multilayer

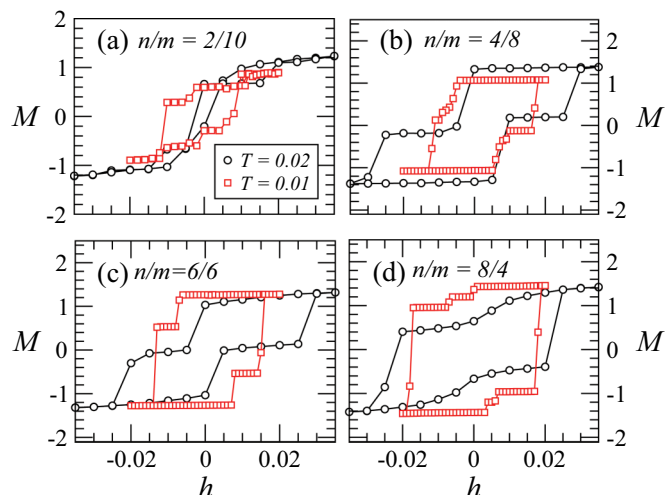


FIG. 4. Magnetization as a function of applied magnetic field with $J_{Mn} = -20$, $J_{Ru} = 4$, $t_l = 0.5$. Results are obtained on 4×12 lattices, with n rows of LAMO and m rows of SRO, with $(n + m) = 12$.

system, we find that the total moment decreases when $T \lesssim T_c^{SRO}$, indicating that the SRO moment is oriented opposite to that of LAMO. This behavior is in good agreement with experimental results [6]. We further support this picture by computing M - h hysteresis curves at low temperatures as shown in Fig. 4. The double-loop feature in the M - h curves also agrees well with experiments [6,7]. It reflects a two-step switching process as a function of h , i.e., LAMO layers align along the field first, while SRO layers align at a stronger field.

III. QUANTUM WELL MODEL

We rationalize our results for the interlayer coupling in multilayers within a quantum well picture; we will later extend these arguments to make predictions for bilayers. To understand the interlayer coupling, we focus on temperatures immediately above $T_c^{SRO} \sim 150$ K. In this regime, the LAMO layers have already developed ferromagnetic order; we assume that their magnetic moment has formed along the “up” direction. The conduction electrons inside the LAMO layers are spin polarized with spins pointing up, as LAMO is a conventional “majority-carrier” ferromagnet. Within our minimal quantum well picture, we assume maximum spin polarization, i.e., down-spin electrons are not present inside the LAMO layers.

Let us first consider SRO-LAMO multilayers as depicted in Fig. 5(a). Each SRO layer can now be thought of as a two-dimensional (2D) quantum well for down electrons. The boundary conditions are set by the adjacent LAMO layers—up electrons can diffuse freely into LAMO layers while down electrons cannot. The down-spin electrons are localized within 2D quantum wells, while the up electrons move freely within a three-dimensional (3D) system. We find the density of states at the Fermi level (DOS) for each spin species taking the electronic dispersion to be that of a free particle in a quantum well with the appropriate width. The up electrons occupy states that are described by a three-dimensional momentum quantum

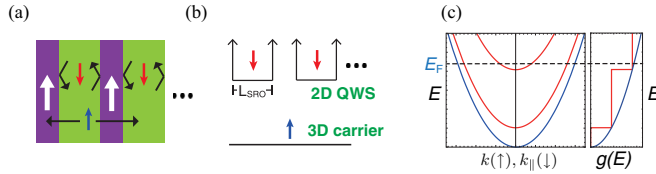


FIG. 5. Quantum well description of SRO-LAMO multilayers: (a) Multilayer geometry, showing spin polarization just above T_c^{SRO} , assuming that the LAMO layers have ordered along the up direction. (b) Potentials seen by the two spin species; the up electrons can diffuse throughout while the down electrons are confined to the SRO layers. (c) The resulting band energies and DOS for the two spin species.

number. The down electrons, however, have one momentum component (k_{\perp}) quantized due to the finite width of the 2D quantum wells. Their dispersion, as shown in Fig. 5(c), forms bands corresponding to each k_{\perp} value. The DOS of both spin species is shown in Fig. 5(c) with the up electrons always having higher DOS. As we are just above T_c^{SRO} , incipient ferromagnetic correlations arise inside each SRO layer. As SRO is a minority-carrier ferromagnet, the higher density of up-spin conduction electrons forces the magnetic moment of SRO to point down. This explains the antiferromagnetic coupling seen in LAMO-SRO multilayers.

The situation is more nuanced in LAMO-SRO bilayers, depicted in Fig. 6(a). In this case, both up and down electrons reside in 2D quantum wells; however, the widths of the two quantum wells are different as shown in Fig. 6(b). The resulting dispersion and DOS are shown in Fig. 6(c). Unlike the multilayer case, the nature of the dominant spin (that with higher DOS) depends on the precise value of the Fermi energy. If up spin has higher DOS, we expect SRO to order with a moment pointing down and vice versa. This paves the way for a falsifiable signature of our conduction-electron driven mechanism. It is somewhat difficult to tune the Fermi energy

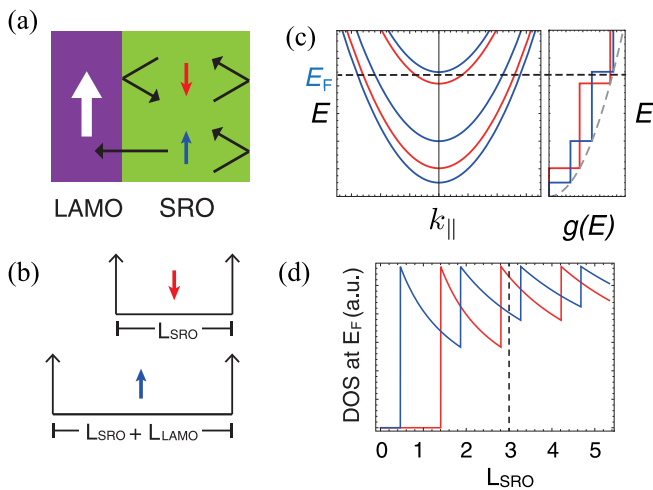


FIG. 6. Quantum well description of SRO-LAMO bilayers: (a) bilayer geometry, (b) potentials seen by the two spin species; the up electrons see a wider quantum well, (c) the resulting band energies and DOS for the two spin species, and (d) DOS vs width of SRO layer, keeping L_{LAMO} fixed at unity. The DOS is shown for an arbitrarily chosen Fermi energy.

TABLE I. Energies in LSMO/SRO bilayers. The preferred magnetic structures are underlined.

SRO/LSMO (u.c.)	Coupling	Total energy (eV)
4/3 u.c.	<u>AFM</u>	-783.6546
	FM	-782.8075
4/5 u.c.	AFM	-1072.8563 ^a
	<u>FM</u>	-1086.1658

^aThe calculations for this AFM state are not converged. Its energy was estimated by a perturbative approach using the charge distribution of the nonmagnetic state and fixed bulk spin values for Ru and Mn ions.

in experiments. However, it is relatively easy to make samples with different relative widths of the SRO and LAMO layers. Tuning the relative widths of the layers also changes the nature of the dominant spin as shown in Fig. 6(d). As a consequence, the ordered moment of SRO layers will switch direction. This suggests a smoking gun signature of our carrier-driven mechanism: by varying the relative width of the SRO-LAMO layers, we can change the nature of the interlayer coupling from antiferromagnetic to ferromagnetic. This is in sharp contrast to a superexchange picture in which the coupling only depends on the interface and is insensitive to the widths of the layers.

IV. *AB INITIO* RESULTS FOR LSMO/SRO BILAYER

We have performed first-principle electronic structure calculations to check for the smoking gun signature suggested by the quantum well picture. Indeed, our *ab initio* simulations show that the nature of the coupling changes upon tuning relative layer width. This provides *a posteriori* support for the arguments in Sec. III above, demonstrating that the quantum well picture successfully captures the essential physics.

LSMO/SRO bilayers have been studied experimentally as well as from an *ab initio* perspective. They have largely been found to be antiferromagnetically coupled. However, only a few values of relative layer widths have been explored. For instance, Ref. [9] found antiferromagnetic coupling in bilayers with widths 16.5/24 nm for LSMO/SRO layers.

We have studied SRO/LSMO bilayers with 4/3 and 4/5 unit cell thicknesses (details described in Appendix A). We find that the bilayer with 4/5 unit cell thicknesses favors ferromagnetic coupling, while that with 4/3 unit cell thicknesses favors antiferromagnetic coupling (see Table I). As antiferromagnetic coupling has been already reported in multiple studies, we present results for the 4/5 bilayer below; the results for the 4/3 bilayer are shown in Appendix B. The structure used for simulations is shown in Fig. 7. We consider an $\text{SrRuO}_3/\text{La}_{2/3}\text{Sr}_{1/3}\text{MnO}_3$ (SRO/LSMO) bilayer on a

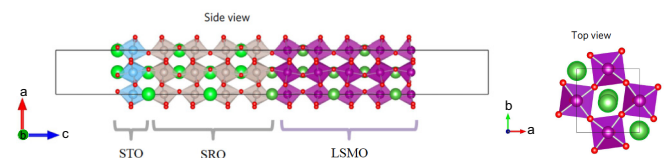


FIG. 7. Lattice structure of a SRO(4 ML)/LSMO(5 ML) bilayer on a STO layer.

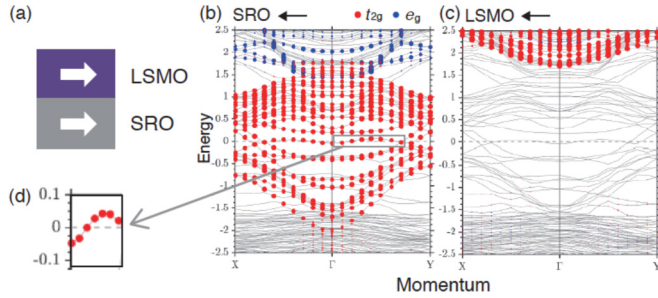


FIG. 8. The projected band structures of a ferromagnetically aligned SRO (4 u.c.)/LSMO (5 u.c.) bilayer. We force both layers to be polarized along the “right” direction as shown in (a). (b) and (c) Electronic band structure as a function of momentum along the bilayer. Both figures show the same dispersion—while (b) shows the Ru orbital weights in each band, (c) shows the orbital weights of Mn. The color denotes the t_{2g} and e_g contributions from Ru atoms in SRO (b) and from Mn atoms of the LSMO layer (c). In both cases, we only show the weight of “left” spin electrons; this is the minority species in LSMO and the majority species in SRO. As LSMO is a majority carrier ferromagnet, we do not find any minority spin contribution to the states near the Fermi level. (d) One of the bands, dominated by Ru t_{2g} electrons, crosses the Fermi level. It is holelike and approximately parabolic.

(001)-SrTiO₃ (STO) substrate (see Fig. 1). The SRO/LSMO layers are taken to be 4/5 unit cells thick. The lattice structure of SRO is orthorhombic [9].

To determine the magnetic configuration with lowest energy, we perform electronic structure simulations with imposed ferromagnetic and antiferromagnetic ordering as shown in Figs. 8 and 9, respectively. In both cases, we find that the degeneracy of t_{2g} and e_g orbitals is broken. This is due to hybridization between layers, confinement in the z direction, as well as the orthorhombic lattice structure of SRO. Therefore, orbital degeneracy does not play an important role.

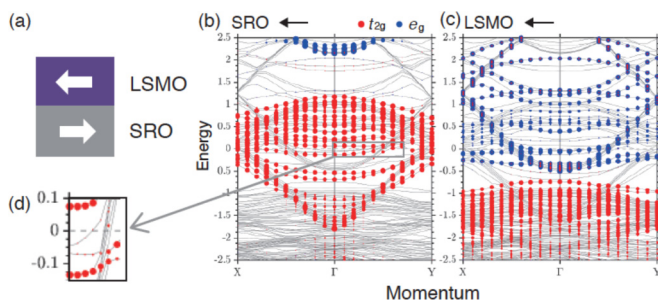


FIG. 9. Band structures of an antiferromagnetically aligned SRO (4 u.c.)/LSMO (5 u.c.) bilayer, with magnetization as shown in (a). (b) and (c) Both show the same band structure. While (b) shows the orbital contribution of Ru d orbitals, (c) shows that of Mn orbitals. In both cases, we show the weight of “left” spins which is the majority species in both layers. The states near the Fermi level are composed of both Ru t_{2g} electrons and Mn e_g electrons, as antiferromagnetic alignment allows these states to hybridize. (d) The band that crossed the Fermi surface in the ferromagnetic case is now pushed up. As a consequence, the ferromagnetic state has lower energy.

In the ferromagnetic configuration, the SRO-minority carriers cannot diffuse into the LSMO side as their energy is aligned with the band gap of LSMO as shown in Figs. 8(b) and 8(c). They are confined within the SRO layer to form quantum well-like bands, which are approximately parabolic. One of these bands intersects the Fermi level, see Fig. 8(d).

In the antiferromagnetically coupled system, the SRO-minority carriers hybridize with LSMO bands. States at the Fermi level have large Ru t_{2g} and Mn e_g contributions. In fact, we find significant Mn t_{2g} components [see red dots on blue bands in Fig. 9(c)] which arise due to hybridization with SRO. This hybridization shifts the quantum well-like bands inside SRO away from the Fermi level [see Fig. 3(d)] to decrease the DOS at Fermi level. Both Figs. 8 and 9 show the band structure of only one spin species, viz., the spin that is opposite to the net magnetic moment of the SRO layer. This is the dominant species within SRO. The dispersion of the other species is shown in Appendix B.

Finally, the energy of the ferromagnetically coupled bilayer (-1086.1658 eV/unit cell) is lower than that of the antiferromagnetically coupled (-1072.8563 eV/unit cell) bilayer. This supports our carrier-driven mechanism indicating that ferromagnetic coupling can be achieved by changing the relative width in the bilayer. A recent experimental study in a SRO/LSMO bilayer has observed that antiferromagnetic coupling vanishes when LSMO thickness is changed. Our study explains this feature [23].

V. DISCUSSION

We have proposed a carrier-driven mechanism for inter-layer coupling in ferromagnetic heterostructures. We have illustrated this using SRO-LAMO bilayers and multilayer heterostructures as suitable test cases. For the multilayer case, we have presented a theoretical model amenable to semiclassical simulations. The model qualitatively reproduces key experimental results without invoking interface-based mechanisms such as superexchange. This strongly supports our picture of carrier-driven coupling.

We have presented a simple theoretical argument, modeling the LAMO and SRO layers as quantum wells. Note that effects of quantum confinement have previously been reported in SRO slabs [24]. Here the density of states within the quantum wells shows spin dependence. Relying on the minority-carrier nature of SRO, we predict the direction of the ordered moment that will develop in SRO. Our results suggest that SRO-LAMO multilayers will always show antiferromagnetic coupling. However, in SRO-LAMO bilayers, we predict that the coupling can be tuned by varying the relative layer widths. This can be easily verified with current experimental setups. We have presented *ab initio* results which support our prediction of oscillating coupling in bilayers. Our results demonstrate that conduction electrons play the central role in determining the interlayer coupling.

Our results show a deep connection between magnetic ordering and spin polarization of charge carriers. This suggests new avenues for manipulating spintronic devices. For instance, a ferromagnetic bilayer can be made antiferromagnetic by injection of a suitably polarized spin current. Alternatively, an antiferromagnetic bilayer can be thought of as a spin-polarized

analog of colossal magnetoresistance. At zero field, a large spin polarized current can flow. When a large enough magnetic field forces the layers to align parallelly, the spin polarization of currents is strongly diminished. Conversely, heterostructure geometries can be tweaked to obtain suitably polarized charge carriers. They can be used as spin filters that can be tuned by an external magnetic field.

ACKNOWLEDGMENTS

C.-H.C., A.H., and H.-T.J. acknowledge support from the National Center for Theoretical Sciences, Taiwan. C.-H.C. acknowledges financial support from the Future and Emerging Technologies (FET) programme within the Seventh Framework Programme for Research of the European Commission under FET-Open Grant No. 618083 (CNTQC).

C.-H.C. and A.H. contributed equally to this work.

APPENDIX A: *AB INITIO* CALCULATIONS

The *ab initio* results presented were obtained from calculations based on the framework of density functional theory (DFT). The VASP package [25–27] was used with the PAW-type pseudopotential [28,29] and PBE-type [30] GGA functional. The DFT+*U* method [31] was considered with the on-site Coulomb repulsion $U = 3.5, 3.0$ eV for Ru [13] and Mn [32] ions, respectively. Self-consistent processes were looped until the total energy converged within 10^{-6} eV in all calculations. The calculations were performed using an $8 \times 8 \times 1$ k mesh, with an energy cutoff of 400 eV. Simple mixing of pseudopotentials of La and Sr ions, known as virtual crystal approximation (VCA) [33], was applied to simulate the doping of cations in $\text{La}_{0.67}\text{Sr}_{0.33}\text{MnO}_3$ layer [34,35]. The supercell structure used had n u.c. of LSMO stacked on m u.c. of SRO on a substrate of 1 u.c. STO (see Fig. 7); this corresponds to the n/m u.c. LSMO/SRO bilayer structure. We considered the close-to-bulk lattice structure for SRO with a $\sqrt{2} \times \sqrt{2}$ perovskite u.c. in the (001) plane [36]. Unlike other magnetic bilayer systems, distortions of oxygen octahedra cannot be ignored here as interactions between Ru- e_g and Mn- t_{2g} orbitals are important in this system.

APPENDIX B: BAND STRUCTURES IN SRO/LSMO BILAYERS

In the main text we discussed the *ab initio* band structure of a SRO (4 u.c.)/LSMO (5 u.c.) bilayer in ferromagnetic/antiferromagnetic configurations. In Figs. 8 and 9 of the main text, we only showed the dispersion of one spin species, the majority species within the SRO layer, as its delocalization is central to our proposed mechanism. Here we show the obtained energy dispersions for the other spin species. In Figs. 10 and 11 we show the band structure for the ferromagnetic and antiferromagnetic configuration, respectively. In the ferromagnetic configuration, as expected, the majority spins of LSMO do not hybridize with SRO states. This is reflected in the band structure in Fig. 10 for the right spin, which has no contribution from SRO orbitals near the Fermi level. In the antiferromagnetic configuration, we see fewer states at the Fermi level with spin right. This can be seen

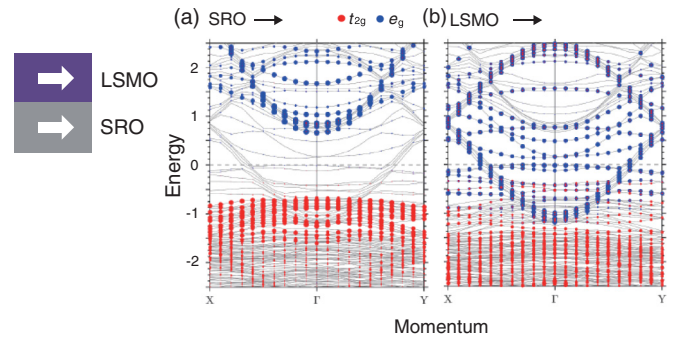


FIG. 10. The projected band structures for the “right” spin species in the ferromagnetically aligned SRO (4 u.c.)/LSMO (5 u.c.) bilayer with parallel magnetic moments pointing right. Both (a) and (b) show the same dispersion. While (a) shows the weight from SRO orbitals, (b) shows the weight from LSMO orbitals.

by contrasting Fig. 11 with Fig. 9 in the main text. The right spin states at the Fermi level are entirely from SRO orbitals as LSMO has strong spin polarization character (majority carrier). The degree of spin polarization in SRO (minority carrier) is not as strong, giving rise to a low density of right spins in Fig. 11.

We have also performed *ab initio* simulations of the SRO (4 u.c.)/LSMO (3 u.c.) bilayer. We find that it prefers antiferromagnetic ordering. The obtained *ab initio* band structures for the ferromagnetic and antiferromagnetic configurations are shown in Figs. 12 and 13, respectively. In each figure we show the dispersions for both spin species. The qualitative features in the band structure are broadly similar to the SRO (4 u.c.)/LSMO (5 u.c.) case. In the ferromagnetic configuration, shown in Fig. 12, neither spin species can delocalize into both layers. The left spin states at the Fermi level are composed of SRO orbitals, while the right states are composed of LSMO orbitals. This is in marked contrast to the antiferromagnetic configuration, shown in Fig. 13, wherein the left spin states at the Fermi level have large SRO and LSMO contributions. This indicates that left spin conduction electrons, forming the minority species in SRO and the majority species in LSMO, are free to delocalize

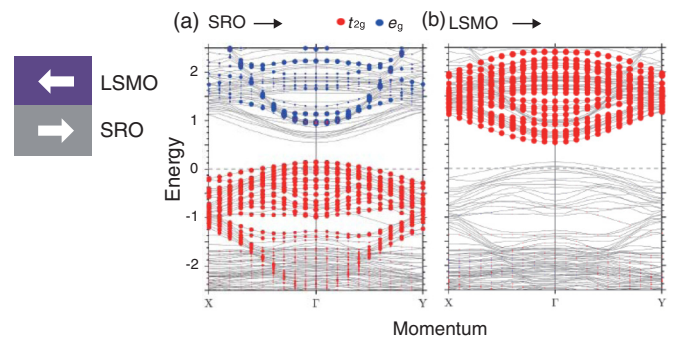


FIG. 11. The projected band structures for the right spin species in the SRO (4 u.c.)/LSMO (5 u.c.) bilayer with antiparallel magnetic moments. Both (a) and (b) show the same dispersion. While (a) shows the weight from SRO orbitals, (b) shows the weight from LSMO orbitals.

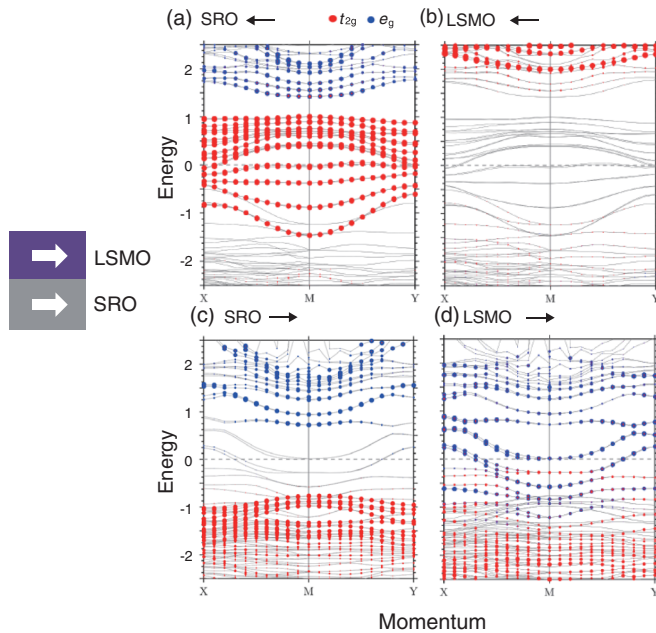


FIG. 12. The projected band structures for the ferromagnetically aligned SRO (4 u.c.)/LSMO (3 u.c.) bilayer. The band structures shown are for (a) “left” spin with SRO orbital contributions shown, (b) left spin with LSMO orbital contributions shown, (c) right spin with SRO orbital contributions shown, and (d) right spin with LSMO orbital contributions shown.

throughout the bilayer. The right spin states are gapped and are pushed down from the Fermi level due to confinement effects.

The obtained band structures strongly support our picture of carrier-driven coupling. At the very least, they show that an interfacial-coupling picture is not tenable as electrons

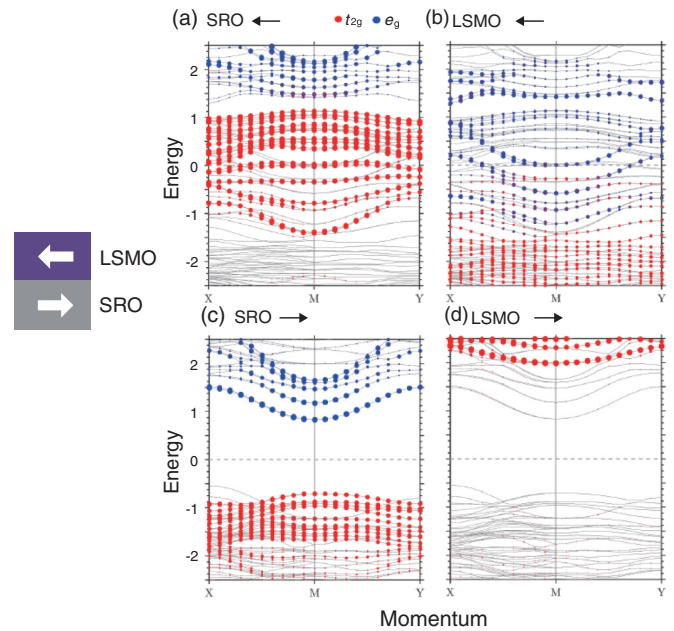


FIG. 13. The projected band structures for the antiferromagnetically aligned SRO (4 u.c.)/LSMO (3 u.c.) bilayer with opposite magnetic moments as shown. The band structures shown are for (a) left spin with SRO orbital contributions shown, (b) left spin with LSMO orbital contributions shown, (c) right spin with SRO orbital contributions shown, and (d) right spin with LSMO orbital contributions shown.

delocalize throughout the sample. More strongly, they show that our simple quantum well argument captures the essential aspects of the band structure. The results confirm the new prediction that arises from the quantum well picture, viz., that the nature of coupling in bilayers can be tuned by changing relative layer width.

- [1] M. Bibes and A. Barthelemy, *IEEE Trans. Electron Devices* **54**, 1003 (2007).
- [2] A. P. Ramirez, *J. Phys.: Condens. Matter* **9**, 8171 (1997).
- [3] H. Y. Hwang, Y. Iwasa, M. Kawasaki, B. Keimer, N. Nagaosa, and Y. Tokura, *Nat. Mater.* **11**, 103 (2012).
- [4] G. Koster, L. Klein, W. Siemons, G. Rijnders, J. S. Dodge, C.-B. Eom, D. H. A. Blank, and M. R. Beasley, *Rev. Mod. Phys.* **84**, 253 (2012).
- [5] D. C. Worledge and T. H. Geballe, *Phys. Rev. Lett.* **85**, 5182 (2000).
- [6] M. Ziese, I. Vrejoiu, E. Pippel, P. Esquinazi, D. Hesse, C. Etz, J. Henk, A. Ernst, I. V. Maznichenko, W. Hergert, and I. Mertig, *Phys. Rev. Lett.* **104**, 167203 (2010).
- [7] A. Solignac, R. Guerrero, P. Gogol, T. Maroutian, F. Ott, L. Largeau, P. Lecoeur, and M. Pannetier-Lecoeur, *Phys. Rev. Lett.* **109**, 027201 (2012).
- [8] D. Feng and G. Jin, *Introduction to Condensed Matter Physics*, Introduction to Condensed Matter Physics No. 1 (World Scientific, Singapore, 2005).
- [9] A. Solignac, R. Guerrero, P. Gogol, T. Maroutian, F. Ott, P. Lecoeur, C. Fermon, and M. Pannetier-Lecoeur, *IEEE Trans. Magn.* **48**, 4363 (2012).
- [10] A. Y. Borisevich, A. R. Lupini, J. He, E. A. Eliseev, A. N. Morozovska, G. S. Svechnikov, P. Yu, Y.-H. Chu, R. Ramesh, S. T. Pantelides, S. V. Kalinin, and S. J. Pennycook, *Phys. Rev. B* **86**, 140102 (2012).
- [11] Y. Lee, B. Caes, and B. Harmon, *J. Alloys Compd.* **450**, 1 (2008).
- [12] P. Mahadevan, F. Aryasetiawan, A. Janotti, and T. Sasaki, *Phys. Rev. B* **80**, 035106 (2009).
- [13] H.-T. Jeng, S.-H. Lin, and C.-S. Hsue, *Phys. Rev. Lett.* **97**, 067002 (2006).
- [14] E. Jakobi, S. Kanungo, S. Sarkar, S. Schmitt, and T. Saha-Dasgupta, *Phys. Rev. B* **83**, 041103 (2011).
- [15] M. Kim and B. I. Min, *Phys. Rev. B* **91**, 205116 (2015).
- [16] H. T. Dang, J. Mravlje, A. Georges, and A. J. Millis, *Phys. Rev. B* **91**, 195149 (2015).
- [17] E. Dagotto, S. Yunoki, A. L. Malvezzi, A. Moreo, J. Hu, S. Capponi, D. Poilblanc, and N. Furukawa, *Phys. Rev. B* **58**, 6414 (1998).
- [18] T. Hotta, *Phys. Rev. B* **67**, 104428 (2003).
- [19] A. J. Millis, P. B. Littlewood, and B. I. Shraiman, *Phys. Rev. Lett.* **74**, 5144 (1995).
- [20] H. Röder, J. Zang, and A. R. Bishop, *Phys. Rev. Lett.* **76**, 1356 (1996).

- [21] S. Kumar and P. Majumdar, *Phys. Rev. Lett.* **96**, 016602 (2006).
- [22] E. Dagotto, T. Hotta, and A. Moreo, *Phys. Rep.* **344**, 1 (2001).
- [23] S. R. Singamaneni, J. T. Prater, and J. Narayan, *Curr. Opin. Solid State Mater. Sci.* **19**, 301 (2015).
- [24] Y. J. Chang, C. H. Kim, S.-H. Phark, Y. S. Kim, J. Yu, and T. W. Noh, *Phys. Rev. Lett.* **103**, 057201 (2009).
- [25] G. Kresse and J. Hafner, *Phys. Rev. B* **48**, 13115 (1993).
- [26] G. Kresse and J. Furthmüller, *Comput. Mater. Sci.* **6**, 15 (1996).
- [27] G. Kresse and J. Furthmüller, *Phys. Rev. B* **54**, 11169 (1996).
- [28] G. Kresse and D. Joubert, *Phys. Rev. B* **59**, 1758 (1999).
- [29] P. E. Blöchl, *Phys. Rev. B* **50**, 17953 (1994).
- [30] J. P. Perdew, K. Burke, and M. Ernzerhof, *Phys. Rev. Lett.* **77**, 3865 (1996).
- [31] A. I. Liechtenstein, V. I. Anisimov, and J. Zaanen, *Phys. Rev. B* **52**, R5467 (1995).
- [32] G. Colizzi, A. Filippetti, and V. Fiorentini, *Phys. Rev. B* **76**, 064428 (2007).
- [33] L. Bellaiche and D. Vanderbilt, *Phys. Rev. B* **61**, 7877 (2000).
- [34] Y. Segal, K. F. Garrity, C. A. F. Vaz, J. D. Hoffman, F. J. Walker, S. Ismail-Beigi, and C. H. Ahn, *Phys. Rev. Lett.* **107**, 105501 (2011).
- [35] Y. W. Yin, J. D. Burton, Y.-M. Kim, A. Y. Borisevich, S. J. Pennycook, S. M. Yang, T. W. Noh, A. Gruverman, X. G. Li, E. Y. Tsymbal, and Q. Li, *Nat. Mater.* **12**, 397 (2013).
- [36] J. M. Rondinelli, N. M. Caffrey, S. Sanvito, and N. A. Spaldin, *Phys. Rev. B* **78**, 155107 (2008).